

Transient coupling modeling and dynamic response analysis of hydraulic turbine governing system and shafting system

Jie Sun, Chen Feng^{*}, Yuquan Zhang^{**}, Yuan Zheng

Hohai University, Nanjing, 210098, China



ARTICLE INFO

Keywords:

Pumped storage power station
Hydraulic turbine governing system
Shafting system vibration
Small oscillation processes
Closure law of guide vanes

ABSTRACT

To address the challenges posed by the connection of new energy sources to the grid, pumped storage power stations (PSPSs) are required to frequently engage in transient processes to maintain load balancing and regulate grid frequency. It remains difficult, however, to evaluate the transient characteristics of the hydraulic turbine governing system (HTGS) and shafting system because of the lack of suitable models. This study seeks to address this challenge by establishing a transient turbine model based on the surface-cluster method and the shafting system transient coupling model, accounting for hydraulic-mechanical-electrical factors. HTGS and shafting systems' dynamic response characteristics are investigated under two small oscillation processes and eleven closure laws of guide vanes (CLGVs). The findings reveal that the shafting system vibration increases with the load drop during small oscillation processes. Conversely, sudden load increases reduce shafting vibration and the change of vibration is related to the force of the blade. Moreover, the study identifies that under the fast-slow two-phase CLGV, the maximum relative head and rotor radial amplitude increase with decreasing guide vanes (GV) opening of the turning point, while the change in maximum relative speed is opposite. Under the slow-fast two-phase CLGV, the maximum head and speed increase with decreasing GV opening of the turning point, while the maximum radial amplitude of the rotor is the opposite. Finally, under all the three-phase CLGVs, the transient characteristics of the head, speed, and shafting vibration under close-close-close (CCC) CLGV are the best. The innovation of this paper is to provide a method to establish the transient coupling model of HTGS and shafting, and to study the stability and transient response characteristics of HTGU.

1. Introduction

Hydroelectric power has been a significant renewable energy source for centuries, but with the impact of climate change and global warming, we must reduce at least 80 % of fossil fuel and biofuel emissions by 2030 for sustainable development [1,2]. According to statistical data, over 90 % of clean and renewable distributed new energy sources have been successfully integrated into the grid [3]. Nevertheless, photovoltaic power generation and wind power generation exhibit intermittency and randomness [4,5], presenting novel challenges to the power grid [6]. To address these challenges, pumped storage power stations (PSHS) need to undergo transient processes more frequently to balance the load and adjust the power system frequency [7–9]. This inevitably results in the transient response of Hydro Turbine Generating Units (HTGU), and variations in turbine flow, speed, and head will induce shaft system vibrations [10,11]. This vibration can cause damage accidents, shorten

the life of HTGU, and result in substantial economic losses [12]. For PSHS to operate safely and reliably, studying the transient behavior of the HTGS and shafting system is essential. Studying the transient process of HTGS requires a comprehensive consideration of pressure pipeline fluctuations [13] and shafting vibrations [14,15].

HTGS is an automated feedback control system comprising a penstock system, hydro-generator unit, and governor. Considerable progress has been achieved in the study of the dynamic models and stability of HTGS in recent years. According to Zhang et al., a linearized reduced-order dynamic model of PSHS was developed by accounting for elastic water columns in pressure pipes. Under random loads, they studied the effect of PI on HTGS dynamics [16]. In Chen et al.'s paper, nonlinear dynamics of hydraulic turbines were investigated using state-space models [17]. Li et al. introduced an improved gravity search algorithm (MGSA) to enhance the parameter identification ability of HTGS [18]. A stochastic model was developed by Guo et al. to analyze

* Corresponding author.

** Corresponding author.

E-mail addresses: windycity@hhu.edu.cn (C. Feng), zhangyq@hhu.edu.cn (Y. Zhang).

the energy distribution in hydropower systems, examining the effects of stochastic intensity on energy conversion during turbine operation [19]. Considering the hydraulic servo's inertia and response time, Gao and Zhang et al. formulated a fast-slow HTGS model, taking the inertia into account while calculating the HTGS. They investigated the fast and slow dynamic behavior of HTGS at different time scales [20,21]. In summary, the current research landscape emphasizes the steady-state characteristics and small oscillation transient features of HTGS, while there is comparatively less focus on the study of transient characteristics during large oscillation transitions [22].

The modeling of the shafting system falls under the purview of rotor dynamics and is influenced by hydraulic, mechanical, and electrical factor [23]. Improved computing power and the finite element method have made shafting modeling possible [24,25]. Karlsson and his colleagues investigated the effects of mechanical power overexcitation on a hydroelectric rotor system in their study [26]. A novel coupled dynamic mathematical model has been developed by Sun et al. that takes into account not only the classical dynamics of nonlinear hydro-generator shafts but also the vibrations of the foundation and random excitations of the foundation [27]. HTGU bending-torsional coupled vibrations are considered in Shi et al.'s mathematical model, and vibration stability and parameter sensitivity are discussed [28]. A dynamic model for an unbalanced rotor-runner bearing system was developed by Zhang et al. using an improved LuGre friction model [29]. With a frequency domain vibration equation, Xie et al. modeled the shaft-foundation coupling system and expressed the thrust bearing's longitudinal stiffness [30]. While mechanical and electrical factors influencing shafting vibration have been comprehensively expounded, hydraulic factors have received limited exploration, primarily owing to their inherent complexity. According to investigations, many hydraulic factors contribute to shafting vibration, including (a) improper combination of runner blade and guide vane number, (b) asymmetrical clearance of the runner's leakage ring, (c) uneven opening of runner blade outlet edge, (d) cavitation of runner blades, (e) blade vortex zone, (f) Karman vortex zone, (g) tail vortex zone, (h) pressure pulsation on the crown of the runner, (i) water diversion asymmetry between volute and seat ring, and (j) manufacturing deviation of flow-passing parts. Due to their intricate relationship with characteristics and operational conditions, the impact of the aforementioned factors on shafting vibration is complex and challenging to articulate. As a result, establishing a mathematical model for the HTGS that incorporates all these factors is inherently difficult.

Consequently, coupling modeling and transient characteristic evaluation of the HTGS and shaft system are challenging [31]. However, a few scholars have addressed this problem and made valuable contributions. In Shi et al.'s study, governor control parameters were analyzed using a nonlinear coupling mathematical model [32]. Under different

load rejection conditions, a combination of water diversion and shafting models were used in the study by Guo et al. [33]. Furthermore, a transient nonlinear coupling model for HTGS and HGSS was developed and various parameters were analyzed with respect to HTGU vibration characteristics under sudden load increases [34]. Notwithstanding the examination of HTGU's vibration characteristics under varied parameters and load disturbances in these studies, their reliance on the traditional turbine model poses a limitation. Whether utilizing the internal characteristic method, the comprehensive characteristic curve, or the six-coefficient equation to depict the turbine model, applying them to the context of large oscillation processes proves challenging, leading to notable cumulative deviations.

Building upon the research context delineated previously, this investigation endeavors to construct a dynamic turbine model predicated on the surface-cluster methodology and the transient coupling model of the shafting system. A fundamental objective of this undertaking is the development of a comprehensive methodology to characterize the transient coupling between the HTGS and the shafting system. This initiative seeks to evaluate the transient response characteristics and their stability, thereby ensuring the secure and reliable operation of the HTGU during transient scenarios.

2. Coupling model of HTGS and shafting system

2.1. Turbine model based on a surface-cluster method

The mathematical depiction of a turbine is conventionally realized via three methodologies: (a) the internal characteristic model, (b) the turbine characteristic curve, and (c) the hydraulic turbine model endorsed by the IEEE [35]. Nevertheless, (a) it necessitates a substantial multitude of unit-specific parameters, and (b) presents shortcomings in the provision of turbine operational data during instances of small opening. The result derived from (c) gives rise to a substantial cumulative disparity, attributable to the inherent approximations inherent in the system's transfer coefficient [36]. Consequently, the imperative lies in the expedited pursuit of refinement in turbine model.

Zhang developed a turbine model using a surface-cluster method to provide more accurate transient characteristics of the HTGS [22]. However, this model has limitations as it only applies to the start-up process. Building on Zhang's work, this paper further enhances the hydraulic turbine transient equation. Fig. 1 (a) illustrates the integral path, using points a, b, c, and d to calculate the torque and discharge value at point d when given the torque and discharge value at point a. It should be noted that a-b represents the equal opening line, b-c represents the equal speed line, and c-d represents the variable head line. Starting from point a, after passing through b and c, the torque and discharge at point

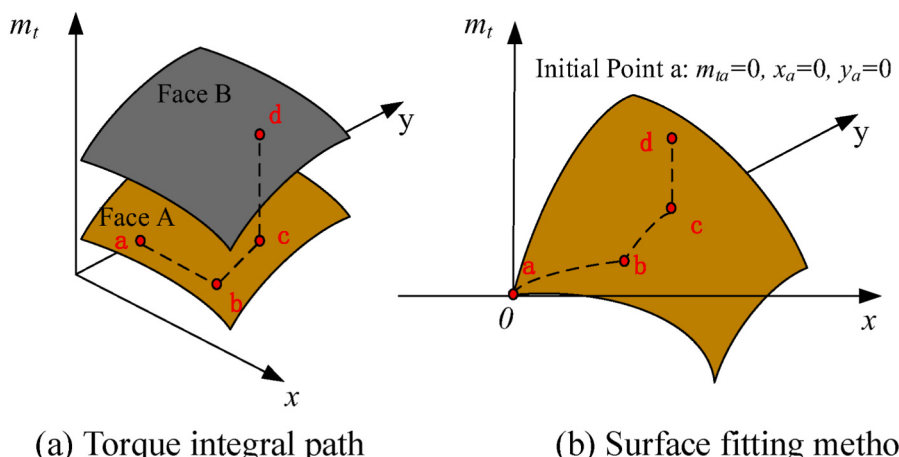


Fig. 1. Torque integral path and surface fitting method of the surface-cluster method (modified from Zhang [22]).

d can be expressed as Eq. (1).

$$\begin{cases} m_{td}(x_d \ y_d \ h_d) = m_{ta}(x_a \ y_a \ h_a) + \int_a^b dm_t + \int_b^c dm_t + \int_c^d dm_t \\ = m_{ta}(x_a \ y_a \ h_a) + \int_{x_a}^{x_d} e_x dx + \int_{y_a}^{y_d} e_y dy + \int_{h_a}^{h_d} e_h dh \\ q_{td}(x_d \ y_d \ h_d) = q_{ta}(x_a \ y_a \ h_a) + \int_a^b dq_t + \int_b^c dq_t + \int_c^d dq_t \\ = q_{ta}(x_a \ y_a \ h_a) + \int_{x_a}^{x_d} e_{qx} dx + \int_{y_a}^{y_d} e_{qy} dy + \int_{h_a}^{h_d} e_{qh} dh \end{cases} \quad (1)$$

The initial value of the integral point a is selected at $x_a = 0, y_a = 0, h_a = 0, m_{ta} = 0, q_{ta} = 0$. It indicates that the initial position is the steady-state operating point of full load under rated conditions, and the change of each state parameter of the system is 0. On the a-b line, $y = 0, h = 0, e_x = e_x(x)$; on the b-c line, $h = 0, e_y = e_y(x, y)$. It is calculated by fitting the characteristic curve of the runner model to determine the transfer coefficient, and it can be expressed as Eq. (2) [37]

$$\begin{cases} e_x = -0.16x - 0.3 \\ e_h = 1.67y \\ e_y = \begin{cases} 1.548(1 - 0.6x), & (0 \leq y < 0.6) \\ 1.2(1 - 0.6x), & (0.6 \leq y < 0.85) \\ 0.385(1 - 0.6x), & (0.85 \leq y \leq 1) \end{cases} \\ e_{qx} = -0.15 \\ e_{qy} = 1.65 - y \\ e_{qh} = 0.17 + 0.4y \end{cases} \quad (2)$$

2.2. Model of hydraulic turbine governing system

The penstocks can be treated as rigid water hammers with a pipeline length less than 600–800 m, as shown in Eq. (4) [38].

$$h = -T_w \dot{q}_t \quad (4)$$

Eq. (5) describes the dynamic characteristics of turbine rotational speed as affected by turbine torque and load torque interactions [39].

$$T_{ab} \ddot{x} + e_n x = m_t - m_g \quad (5)$$

where h is relative deviation of head; \dot{q}_t is derivatives of the flow with respect to time; T_w is the flow inertia time; $T_{ab} = T_a + T_b$, T_a and T_b are inertia time constants of generators and loads; e_n is a comprehensive self-regulation coefficient.

The differential equation of the electro-hydraulic servo system is given by Eq. (6) [40].

$$\dot{y} = \frac{u - y}{T_y} \quad (6)$$

The PID control equation is Eq. (7) [40].

$$\dot{u} = -k_p \dot{x} - k_i x - k_d \ddot{x} \quad (7)$$

where k_p, k_i and k_d are proportional, integral, and differential gain. y is relative deviation of guide vane opening; T_y is the engager relay time constant; u is regulator output.

Servo system amplification and the mechanical inertia of the main servomotor were neglected to ensure modeling accuracy and minimize system complexity [41]. The HTGS transient model is given by Eq. (8).

$$\begin{cases} \dot{x} = \frac{1}{T_{ab}} (m_t - e_n x - m_g) \\ \dot{h} = \frac{(0.17 + 0.4y)(\dot{q} - 1.65\dot{y} + y\dot{y} + 0.15\dot{x}) - (0.4q\dot{y} - 0.66y\dot{y} + 0.2\dot{y}y^2 + 0.06x\dot{y})}{(0.17 + 0.4y)^2} \\ \dot{y} = \frac{u - y}{T_y} \\ \dot{u} = -k_p \dot{x} - k_i x - k_d \ddot{x} \\ \dot{q}_t = -\frac{(q_t - 1.65y + 0.5y^2 + 0.15x)}{(0.17 + 0.4y)T_w} \\ \dot{m}_t = \begin{cases} -0.16x\dot{x} - 0.3\dot{x} + 1.67\dot{y}h + 1.67y\dot{h} + 1.548[(1 - 0.6x)\dot{y} - 0.6\dot{x}y] & (0 \leq y < 0.6) \\ -0.16x\dot{x} - 0.3\dot{x} + 1.67\dot{y}h + 1.67y\dot{h} + 1.2[(1 - 0.6x)\dot{y} - 0.6\dot{x}y] & (0.6 \leq y < 0.85) \\ -0.16x\dot{x} - 0.3\dot{x} + 1.67\dot{y}h + 1.67y\dot{h} + 0.385[(1 - 0.6x)\dot{y} - 0.6\dot{x}y] & (0.85 \leq y \leq 1) \end{cases} \end{cases} \quad (8)$$

An improved surface-cluster model can more accurately describe the transient characteristics of turbine torque and discharge as follows:

$$\begin{cases} m_t(x \ y \ h) = \begin{cases} -0.08x^2 - 0.3x + 1.67yh + 1.548(1 - 0.6x)y & (0 \leq y < 0.6) \\ -0.08x^2 - 0.3x + 1.67yh + 1.2(1 - 0.6x)y & (0.6 \leq y < 0.85) \\ -0.08x^2 - 0.3x + 1.67yh + 0.385(1 - 0.6x)y & (0.85 \leq y \leq 1) \end{cases} \\ q_t(x \ y \ h) = 1.65y - 0.5y^2 - 0.15x - (0.17 + 0.4y)h \end{cases} \quad (3)$$

where h, q, x, y, m_t, m_g are relative values. $h = (H - H_0)/H_0, x = (N - N_0)/N_0, q = (Q - Q_0)/Q_0, m_t = (M_t - M_{t0})/M_{t0}, y = (Y - Y_0)/Y_0, m_g = (M_g - M_{g0})/M_{g0}$.

2.3. Shafing system vibration mathematical model

2.3.1. Damping

The damping force in a stable hydro-generator unit can be expressed mathematically as [42]:

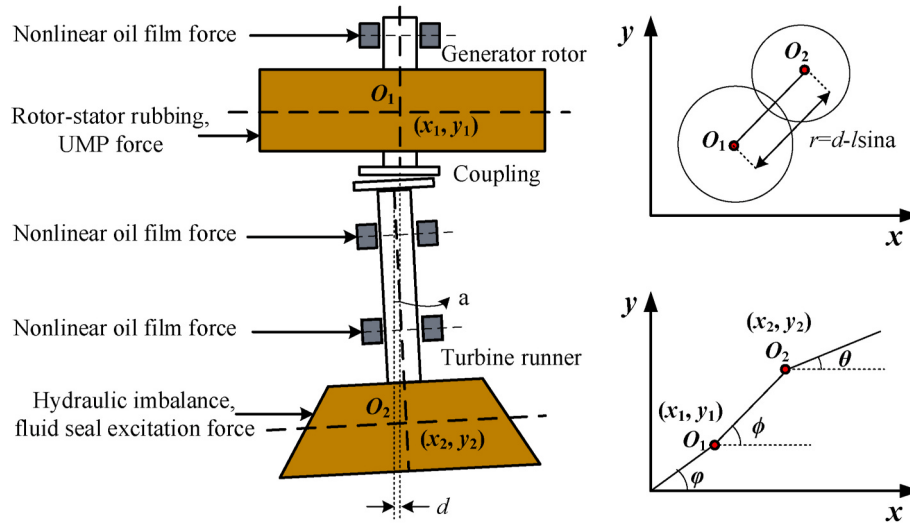


Fig. 2. Schematic diagram and coordinate position diagram of shafting misalignment.

$$\begin{cases} F_{x_damp} = -c\dot{x}_1 \\ F_{y_damp} = -c\dot{y}_1 \end{cases} \quad (9)$$

2.3.2. Rotor-stator rubbing

Given that the collision between the rotor and stator is elastic and that no thermal effect occurs during rotor motion, the friction can be expressed as Eq. (10) [43–45].

$$\begin{cases} F_{x_rub} = -H_1 \frac{(r_1 - \delta)}{r_1} k_r (x_1 - f y_1) \\ F_{y_rub} = -H_1 \frac{(r_1 - \delta)}{r_1} k_r (y_1 + f x_1) \end{cases} \quad (10)$$

where δ is the initial rotor-stator clearance. k_r is the stator radial stiffness; $r_1 = \sqrt{x_1^2 + y_1^2}$. f is the friction coefficient. H_1 is a switching function. The Eq. is as follows (11)

$$H_1 = 0.5 \text{sign}[abs(r_1 - \delta)] + 0.5 \text{sign}(r_1 - \delta) \quad (11)$$

2.3.3. UMP

UMP is caused by the non-uniform magnetic field of the generator rotor, which amplifies the transfer eccentricity effect. The UMP equation is as follows [46]:

$$\begin{cases} F_{x_ump} \\ F_{y_ump} \end{cases} = \frac{RL\pi k^2 I_j^2}{4\mu_0 r_1} (2\Lambda_0\Lambda_1 + \Lambda_1\Lambda_2 + \Lambda_2\Lambda_3) \begin{cases} x_1 \\ y_1 \end{cases} \quad (12)$$

$$\begin{cases} \Lambda_0 = \frac{\mu_0}{\delta_0} \frac{1}{\sqrt{1-\varepsilon^2}} \\ \Lambda_1 = \frac{2\mu_0}{\delta_0} \frac{1}{\sqrt{1-\varepsilon^2}} \left[\frac{1-\sqrt{1-\varepsilon^2}}{\varepsilon} \right] \\ \Lambda_2 = \frac{2\mu_0}{\delta_0} \frac{1}{\sqrt{1-\varepsilon^2}} \left[\frac{1-\sqrt{1-\varepsilon^2}}{\varepsilon} \right]^2 \\ \Lambda_3 = \frac{2\mu_0}{\delta_0} \frac{1}{\sqrt{1-\varepsilon^2}} \left[\frac{1-\sqrt{1-\varepsilon^2}}{\varepsilon} \right]^3 \end{cases} \quad (13)$$

where R and L are the generator rotor radius and length, respectively. k_j is the fundamental magneto-motive potential coefficient of an air gap. I_j is the generator excitation current. μ_0 is the air permeability coefficient. Λ_n is the Fourier coefficient of air gap permeance.

2.3.4. Nonlinear oil film

Assuming an incompressible fluid and constant viscosity, we can express the nonlinear oil film forces as follows [47]:

$$\begin{cases} F_{x_oil} \\ F_{y_oil} \end{cases} = -\sigma \frac{[(x_1 - 2\dot{y}_1)^2 + (y_1 + 2\dot{x}_1)^2]^{1/2}}{1 - x_1^2 - y_1^2} \times \begin{cases} 3x_1 V(x_1, y_1, \alpha) - G(x_1, y_1, \alpha) \sin \alpha - 2S(x_1, y_1, \alpha) \cos \alpha \\ 3y_1 V(x_1, y_1, \alpha) + G(x_1, y_1, \alpha) \cos \alpha - 2S(x_1, y_1, \alpha) \sin \alpha \end{cases} \quad (14)$$

$$\begin{cases} V(x_1, y_1, \alpha) = \frac{2 + (y_1 \cos \alpha - x_1 \sin \alpha)G(x_1, y_1, \alpha)}{1 - x_1^2 - y_1^2} \\ S(x_1, y_1, \alpha) = \frac{x_1 \cos \alpha + y_1 \sin \alpha}{1 - (x_1 \cos \alpha + y_1 \sin \alpha)^2} \\ G(x_1, y_1, \alpha) = \frac{2}{(1 - x_1^2 - y_1^2)^{1/2}} \times \left[\frac{\pi}{2} + \arctan \frac{y_1 \cos \alpha - x_1 \sin \alpha}{(1 - x_1^2 - y_1^2)^{1/2}} \right] \\ \alpha = \arctan \frac{y_1 + 2\dot{x}_1}{x_1 - 2\dot{y}_1} - \frac{\pi}{2} \text{sign} \left[\frac{y_1 + 2\dot{x}_1}{x_1 - 2\dot{y}_1} \right] - \frac{\pi}{2} \text{sign}(y_1 + 2\dot{x}_1) \\ \sigma = \mu \omega R_b L_b \left(\frac{R_b}{h_{oil}} \right)^2 \left(\frac{L_b}{2R_b} \right)^2 \end{cases} \quad (15)$$

where α is the initial dynamic boundary angle of the oil film. σ is the Sommerfeld correction number. μ is oil film viscosity. h_{oil} is oil film thickness. R_b and L_b are the bearing radius and length.

2.3.5. Hydraulic imbalance

Hydraulic factors can cause shaft vibration, which may lead to a non-uniform flow section and result in a non-zero sum of radial water thrust [44]. As described by Shi et al. [43,48], the circular motion of the flow at the seal causes a hydraulic imbalance force.

$$\begin{cases} F_{x_hub} = -\zeta_0 Q \frac{\rho}{A} (v_2 \cos \beta_2 - v_1 \cos \beta_1) e_2^2 \cos \omega t \\ F_{y_hub} = -\zeta_0 Q \frac{\rho}{A} (v_2 \cos \beta_2 - v_1 \cos \beta_1) e_2^2 \sin \omega t \end{cases} \quad (16)$$

where ζ_0 is turbulence coefficient; β_1, β_2 are flow inlet and outlet angle, respectively. A is the cross-sectional area, $A = \pi \left(\frac{R_1+R_2}{2}\right)^2$. R_1 and R_2 are blade inlet radius and lower ring outlet radius, respectively. v_1 and v_2 are blade inlet and outlet velocities. $v_1 = Q/(\pi R_1^2)$, $v_2 = Q/(\pi R_2^2)$.

Eq. (17) can be used to calculate the hydraulic imbalance force caused by uneven opening of turbine blade outlet edges by Xu et al. [49], A_1, A_2 can be expressed using Eq. (18).

$$\begin{cases} F_{x_blade} = \frac{\gamma C_y F |\cos \alpha|}{2g \cos \lambda} [A_1 \cos(\beta_{m1} - \lambda) - A_2 \cos(\beta_{m2} - \lambda)] \\ F_{y_blade} = \frac{\gamma C_x F |\sin \alpha|}{2g \cos \lambda} [A_1 \cos(\beta_{m1} - \lambda) - A_2 \cos(\beta_{m2} - \lambda)] \\ A_1 = \frac{Q^2}{(s_1 \pi D_1^2 \sin \beta_1)^2} + \frac{Q^2}{(s_2 \pi D_2^2 \sin \beta_{21})^2} + \frac{2Q^2 \cos(\beta_1 - \beta_{21})}{s_1 s_2 \pi^2 D_1^2 D_2^2 \sin \beta_1 \sin \beta_{21}} \\ A_2 = \frac{Q^2}{(s_1 \pi D_1^2 \sin \beta_1)^2} + \frac{Q^2}{(s_2 \pi D_2^2 \sin \beta_{22})^2} + \frac{2Q^2 \cos(\beta_1 - \beta_{22})}{s_1 s_2 \pi^2 D_1^2 D_2^2 \sin \beta_1 \sin \beta_{22}} \end{cases} \quad (17)$$

Where γ is the weight of water; C_y is the lift coefficient of the runner blade; C_x is the damping coefficient of the runner blade; α is the blade angle; $\lambda = \arctan(C_x/C_y)$; β_{m1} is the convected velocity; β_{m2} is the convected velocity for other blades; s_1, s_2 represent the reduction in flow over the cross-section of the blade due to the thickness of the blade at the inlet and outlet, respectively. β_{21} is the angle between the relative velocity and the circumferential direction of blade; β_{22} is the angle between the relative velocity and the circumferential direction of convected velocity; D_1, D_2 are the diameter of the runner at the inlet and outlet.

In addition to the hydraulic imbalance force, which is proportional to the discharge, there is also a pressure pulsation induced by the periodic variation of the seal gap caused by the non-circular runner or the

Where k_w is the coefficient of hydraulic imbalance force; ξ usually takes 180° .

2.3.6. Fluid seal excitation

According to Xu et al. [51], the fluid excitation force in the annular seal may lead to rotor instability. Therefore, this paper introduces the Muszynska model to represent the sealing force, as shown in Eq. (20).

$$\begin{cases} F_{x_sf} = -\left(K - m_f \tau_f^2 \omega^2\right)x_1 - \tau_f \omega D_s y_1 - D_s \dot{x}_1 - 2\tau_f m_f \omega \dot{y}_1 - m_f \ddot{x}_1 \\ F_{y_sf} = -\left(K - m_f \tau_f^2 \omega^2\right)y_1 + \tau_f \omega D_s x_1 - D_s \dot{y}_1 + 2\tau_f m_f \omega \dot{x}_1 - m_f \ddot{y}_1 \end{cases} \quad (20)$$

where ω is the angular velocity; K is the sealing force equivalent stiffness; D_s is the equivalent damping of sealing force; m_f is the equivalent mass of sealing force. K, D_s, τ_f are nonlinear functions of perturbation displacements x_1, y_1 .

2.3.7. Shafting vibration mathematical model

The Lagrangian function can be expressed as Eq. (21)

$$\begin{aligned} L = & T - U \\ = & \frac{1}{2} (J_1 + m_1 e_1^2) \dot{\theta}^2 + \frac{1}{2} [J_2 + m_2 (r^2 + e_2^2)] \dot{\theta}^2 - \frac{1}{2} k_2 (x_1^2 + y_1^2 + 2r x_1 \cos \theta + 2r y_1 \sin \theta + r^2) \\ & + \frac{1}{2} m_1 (\dot{x}_1^2 + \dot{y}_1^2 + e_1^2 \dot{\theta}^2 - 2\dot{x}_1 e_1 \dot{\theta} \sin \theta + 2\dot{y}_1 e_1 \dot{\theta} \cos \theta) - \frac{1}{2} k_1 (x_1^2 + y_1^2) \\ & + \frac{1}{2} m_2 (\dot{x}_2^2 + \dot{y}_2^2 + e_2^2 \dot{\theta}^2 - 2\dot{x}_2 e_2 \dot{\theta} \sin \theta + 2\dot{y}_2 e_2 \dot{\theta} \cos \theta) \end{aligned} \quad (21)$$

where $\varphi = \omega t + \varphi_0$, $\theta = \omega t + \theta_0$. φ_0, θ_0 are the initial phases of the generator rotor and turbine runner. Here consider $\varphi_0 = 0, \theta_0 = 0$. $\Sigma F_x, \Sigma F_y$ is the external force on the x, y direction of the shafting.

According to the diagram presented in Fig. 2, the coordination relationship between x_1 and x_2 can be obtained. $x_2 = x_1 + (d - l \sin a) \cos \varphi, y_2 = y_1 + (d - l \sin a) \sin \varphi$. $\varphi = \omega t + \varphi_0, \varphi_0 = 0$.

When calculating, let $\dot{x}_2 = \dot{x}_1 - (d - l \sin a) \omega \sin \omega t, \dot{y}_2 = \dot{y}_1 + (d - l \sin a) \cos \omega t$. d and a are the misalignment amount and angle. l is the shaft length of the turbine. A shafting system vibration mathematical model, such as Eq. (22), can be obtained.

$$\begin{cases} \ddot{x}_1 = \left\{ \begin{array}{l} \Sigma F_x + [(m_1 e_1 + m_2 e_2) \sin \omega t + m_2 (d - l \sin a) \sin \omega t] \dot{\theta} - (k_1 + k_2) x_1 \\ + [(m_1 e_1 + m_2 e_2) \cos \omega t + m_2 (d - l \sin a) \cos \omega t] \dot{\theta} - k_2 (d - l \sin a) \cos \omega t \end{array} \right\} / (m_1 + m_2) \\ \ddot{y}_1 = \left\{ \begin{array}{l} \Sigma F_y - [(m_1 e_1 + m_2 e_2) \cos \omega t + m_2 (d - l \sin a) \cos \omega t] \dot{\theta} - (k_1 + k_2) y_1 \\ + [(m_1 e_1 + m_2 e_2) \sin \omega t + m_2 (d - l \sin a) \sin \omega t] \dot{\theta} - k_2 (d - l \sin a) \sin \omega t \end{array} \right\} / (m_1 + m_2) \\ \ddot{x}_2 = \ddot{x}_1 - (d - l \sin a) (\omega^2 \cos \omega t + \dot{\theta} \sin \omega t) \\ \ddot{y}_2 = \ddot{y}_1 + (d - l \sin a) (\dot{\theta} \cos \omega t - \omega^2 \sin \omega t) \\ \Sigma F_x = F_{x_damp} + F_{x_rub} + F_{x_ump} + F_{x_oil} + F_{x_hub} + F_{x_sf} + F_{x_blade} + F_{x_pul} \\ \Sigma F_y = F_{y_damp} + F_{y_rub} + F_{y_ump} + F_{y_oil} + F_{y_hub} + F_{y_sf} + F_{y_blade} + F_{y_pul} \end{cases} \quad (22)$$

oscillation [50]. The pulsation can be expressed as follows:

$$\begin{cases} F_{x_pul} = k_w \cos(\omega t + \xi) x \\ F_{y_pul} = k_w \cos(\omega t + \xi) y \end{cases} \quad (19)$$

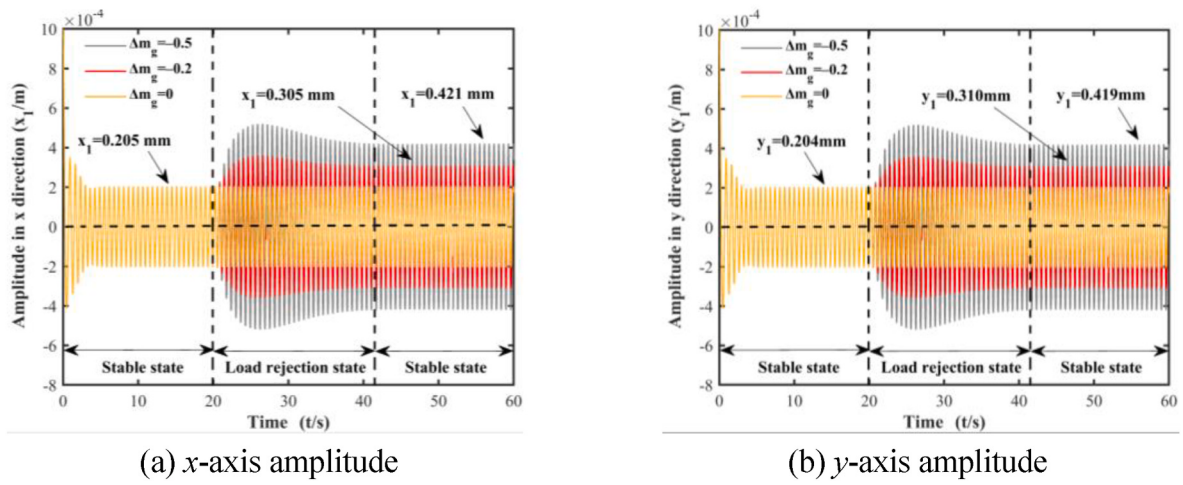


Fig. 3. Shafting vibration at 0 %, 20 %, and 50 % load rejection.

2.4. Coupling model of HTGS and shafting system

Shafting must be coupled with HTGS model by determining how the former influences the latter. The torque equation based on fixed blade lift and drag coefficients was used by Guo to connect them [33]. Nevertheless, since the blade lift and drag coefficients alter incessantly during the transient phase, it is bound to introduce inaccuracies. This research employs the torque equation derived from the Lagrange formula to achieve the coupling.

As found by Xu et al. [52], torque is inversely proportional to load torque as shown by Eq. (23).

$$(m_t - m_g)M_{gB} = J\dot{\omega} + A\ddot{x}_1 + B\ddot{y}_1 + C \quad (24)$$

$$\begin{cases} J = J_1 + J_2 + 2m_1e_1^2 + 2m_2e_2^2 + 2m_2(d - l \sin a)^2 + 2m_2e_2(d - l \sin a)\cos \omega t \\ A = -[(m_1e_1 + m_2e_2)\sin \omega t + m_2(d - l \sin a)\sin \omega t] \\ B = (m_1e_1 + m_2e_2)\cos \omega t - m_2(d - l \sin a)\cos \omega t \\ C = -k_2(d - l \sin a)(x_1 \sin \omega t - y_1 \cos \omega t) \end{cases} \quad (25)$$

The change of $m_t - m_g$ leads to the change of $\dot{\omega}$, which influences the

$$\begin{aligned} M_t - M_g &= \frac{d}{dt} \left(\frac{\partial L}{\partial \dot{\phi}} \right) - \frac{\partial L}{\partial \phi} \\ &= [J_1 + J_2 + 2m_1e_1^2 + 2m_2e_2^2 + 2m_2(d - l \sin a)^2 + 2m_2e_2(d - l \sin a)\cos \omega t] \dot{\omega} - k_2(d - l \sin a)(x_1 \sin \omega t - y_1 \cos \omega t) - [(m_1e_1 + m_2e_2)\sin \omega t + m_2(d - l \sin a)\sin \omega t]\ddot{x}_1 \\ &\quad + [(m_1e_1 + m_2e_2)\cos \omega t - m_2(d - l \sin a)\cos \omega t]\ddot{y}_1 \end{aligned} \quad (23)$$

where $M_t = m_t M_{gB}$, $M_g = m_g M_{gB}$. M_{gB} is a basic value of the generator

vibration. Therefore, $m_t - m_g = T_{ab} \frac{dx}{dt} + e_n x$ can be brought to Rewrite $\dot{\omega}$, as shown in Eq. (26).

$$\begin{aligned} \dot{\omega} &= \frac{(T_{ab}\dot{x} + e_n x)M_{gB} - A\ddot{x}_1 - B\ddot{y}_1 - C}{J} \\ &= \frac{\left\{ (T_{ab}\dot{x} + e_n x)M_{gB} + [(m_1e_1 + m_2e_2)\sin \omega t + m_2(d - l \sin a)\sin \omega t]\ddot{x}_1 \right. \\ &\quad \left. - [(m_1e_1 + m_2e_2)\cos \omega t - m_2(d - l \sin a)\cos \omega t]\ddot{y}_1 - k_2(d - l \sin a)(x_1 \sin \omega t - y_1 \cos \omega t) \right\}}{J_1 + J_2 + 2m_1e_1^2 + 2m_2e_2^2 + 2m_2(d - l \sin a)^2 + 2m_2e_2(d - l \sin a)\cos \omega t} \end{aligned} \quad (26)$$

torque.

Transform Eq. (23) and rewrite it to the Eq. (24), and J, A, B, C can be expressed as Eq. (25).

The transient coupling model can be represented by Eq. (27).

$$\left\{ \begin{array}{l} \dot{x} = \frac{1}{T_{ab}}(m_t - e_n x - m_g) \\ \dot{q}_t = -\frac{(q_t - 1.65y + 0.5y^2 + 0.15x)}{(0.17 + 0.4y)T_w} \\ \dot{h} = \frac{(0.17 + 0.4y)(q_t - 1.65y + yy + 0.15\dot{x}) - (0.4q_t - 0.66yy + 0.2yy^2 + 0.06xy)}{(0.17 + 0.4y)^2} \\ \ddot{m}_t = \begin{cases} -0.16x\ddot{x} - 0.3\dot{x} + 1.67y\ddot{y} + 1.67y\dot{h} + 1.548[(1 - 0.6x)\dot{y} - 0.6\dot{xy}] & (0 \leq y < 0.6) \\ -0.16x\ddot{x} - 0.3\dot{x} + 1.67y\ddot{y} + 1.67y\dot{h} + 1.2[(1 - 0.6x)\dot{y} - 0.6\dot{xy}] & (0.6 \leq y < 0.85) \\ -0.16x\ddot{x} - 0.3\dot{x} + 1.67y\ddot{y} + 1.67y\dot{h} + 0.385[(1 - 0.6x)\dot{y} - 0.6\dot{xy}] & (0.85 \leq y \leq 1) \end{cases} \\ \dot{y} = \frac{u - y}{T_y} \\ \dot{u} = -k_p\dot{x} - k_i x - k_d\ddot{x} \\ \ddot{x}_1 = \left\{ \begin{array}{l} \Sigma F_x + [(m_1 e_1 + m_2 e_2) \sin \omega t + m_2(d - l \sin a) \sin \omega t] \frac{(T_{ab}\dot{x} + e_n x)M_{gB} - A\ddot{x}_1 - B\ddot{y}_1 - C}{J} \\ + [(m_1 e_1 + m_2 e_2) \cos \omega t + m_2(d - l \sin a) \cos \omega t] \omega^2 - (k_1 + k_2)x_1 - k_2(d - l \sin a) \cos \omega t \end{array} \right\} / (m_1 + m_2) \\ \ddot{y}_1 = \left\{ \begin{array}{l} \Sigma F_y - [(m_1 e_1 + m_2 e_2) \cos \omega t + m_2(d - l \sin a) \cos \omega t] \frac{(T_{ab}\dot{x} + e_n x)M_{gB} - A\ddot{x}_1 - B\ddot{y}_1 - C}{J} \\ + [(m_1 e_1 + m_2 e_2) \sin \omega t + m_2(d - l \sin a) \sin \omega t] \omega^2 - (k_1 + k_2)y_1 - k_2(d - l \sin a) \sin \omega t \end{array} \right\} / (m_1 + m_2) \\ \ddot{x}_2 = \ddot{x}_1 - (d - l \sin a) \left(\omega^2 \cos \omega t + \frac{(T_{ab}\dot{x} + e_n x)M_{gB} - A\ddot{x}_1 - B\ddot{y}_1 - C}{J} \sin \omega t \right) \\ \ddot{y}_2 = \ddot{y}_1 + (d - l \sin a) \left(\frac{(T_{ab}\dot{x} + e_n x)M_{gB} - A\ddot{x}_1 - B\ddot{y}_1 - C}{J} \cos \omega t - \omega^2 \sin \omega t \right) \\ \Sigma F_x = F_{x_damp} + F_{x_rub} + F_{x_ump} + F_{x_oil} + F_{x_hub} + F_{x_lf} + F_{x_blade} + F_{x_pul} \\ \Sigma F_y = F_{y_damp} + F_{y_rub} + F_{y_ump} + F_{y_oil} + F_{y_hub} + F_{y_lf} + F_{y_blade} + F_{y_pul} \end{array} \right. \quad (27)$$

3. Model verification and calculation parameter

3.1. Verification of shafting vibration values different load fluctuations

Fig. 3 illustrates the shafting vibration of the HTGU under three different load rejections: 0 %, 20 %, and 50 %. Prior to load rejection (0–20 s), the amplitudes of the HTGU on x_1 and y_1 are 0.205 and 0.204 mm, respectively. During the load rejection process (20–42 s), the amplitude initially increases and then decreases. Following load rejection (42–60 s), the amplitude gradually returns to a stable state. It is noteworthy that the amplitude is greater when the load rejection is higher. This study compares numerical results with experimental data and reference material [33] to ensure that the model proposed here is precise and reliable. The results are presented in and Fig. 4.

The average error between the calculated and experimental results is 6.23 %, and that between the calculated results and the references is 4.61 %. This error may be attributed to the inclusion of more factors affecting vibration in this study than in the experiment and reference [33]. Nonetheless, overall, the transient model of the shafting system and HTGS proposed in this study is dependable and capable of reflecting the alterations in shafting vibration during the transition process.

3.2. Calculation parameter

Using a hydropower station with a simple penstock system as an example, this paper analyzes the transition process under the HTGU. A power station's basic parameters are listed in Table 1.

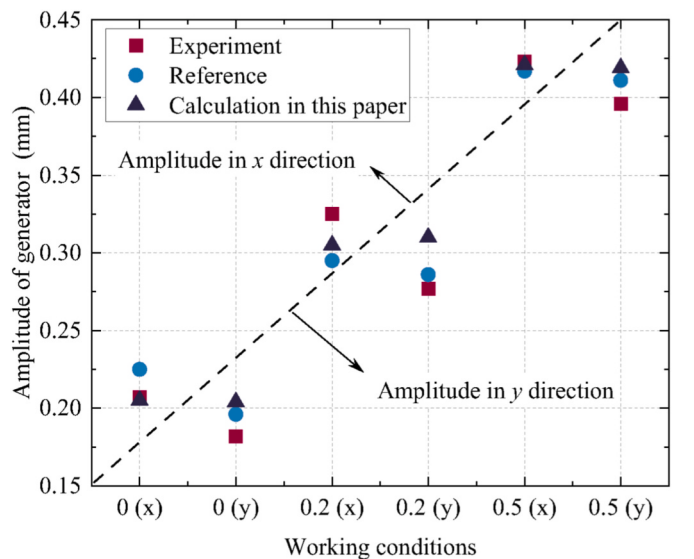


Fig. 4. Shafting vibration comparison of experimental, reference [33], calculation in this paper under different load fluctuations.

Table 1

Power station parameters.

Parameters	value	Parameters	value
Penstock flows inertia time constant T_w [s]	0.8	The inertia time constant T_{ab} [s]	12
Main servomotor time constant T_y [s]	0.02	Proportional gain k_p [-]	3
Generator rotor bearing stiffness k_1 [N/m]	8.5×10^7	Differential gain k_d [s]	3
Hydro-turbine bearing stiffness k_2 [N/m]	8.1×10^7	Runner mass m_2 [kg]	8.1×10^5
Runner mass eccentricity e_2 [m]	0.0003	Integral gain k_i [s^{-1}]	2.75
Stator radial stiffness k_r [N/m]	2.5×10^8	Flow inlet angle β_1 [deg]	16.1
Air gap fundamental magneto-motive potential coefficient k_t [-]	5.1	Flow outlet angle β_2 [deg]	14.2
Unbalanced deflection angle a [deg]	1×10^{-4}	Oil film viscosity μ [Pa·s]	0.018
Generator mass eccentricity e_1 [m]	0.0005	Oil film thickness h_{oil} [m]	1.1×10^{-4}
Damping coefficient c [N·s/m]	4.2×10^5	Generator mass m_1 [kg]	6.9×10^5
Generator excitation current I_j [A]	1000	Friction coefficient f [-]	0.01
Generator rotor average air gap length δ_0 [m]	0.008	Turbine shaft length l [m]	4
Air permeability coefficient μ_0 [H/m]	$4\pi \times 10^{-7}$	Unbalanced alignment d [m]	0.008
Generator torque basic value M_{gb} [N·m]	7.497×10^5	Generator rotor radius R [m]	1.2
Generator rotary inertia J_1 [$kg \cdot m^2$]	7.9×10^6	Generator rotor length L [m]	0.5
Hydro-turbine rotary inertia J_2 [$kg \cdot m^2$]	3.5×10^6		

4. The transient response characteristics of the unit under a small oscillation process

4.1. Sudden load decrease of HTGU

It is assumed that the initial 20 s represent the steady-state condition and that the load suddenly decreases by 5 %, 7.5 %, and 10 % at 20 s. After several cycles of attenuating oscillations, the time-domain response of variables x and h converges to the equilibrium point (Fig. 5(a) and (b)). Before the load decrease, the rotor amplitude in the x direction was 0.205 mm. Upon load reduction by 5 %, 7.5 %, and 10 %, the rotor amplitude increased suddenly, and its maximum amplitude in the x direction reached 0.252 mm, 0.275 mm, and 0.297 mm, respectively, as shown in Fig. 5(c), (d), and (e). After the HTGU re-entered the stability, the amplitude tended to stabilize again but was still higher than before the load change, at 0.233 mm, 0.248 mm, and 0.261 mm, respectively. Furthermore, the amplitude response process in the y direction, shown in Fig. 5(f), is very similar to that in the x direction. The greater the load reduction, the greater the increment of the rotor amplitude.

4.2. Sudden load increase of HTGU

Fig. 6 depicts the transient response processes of relative speed, relative head, and radial vibration of the rotor when the load experiences a sudden increase of 5 %, 7.5 %, and 10 %. As demonstrated in 6

experiencing a significant decline and rise, following the sudden increase in load from a stable state. It is observed that the more the load increases, the smaller the amplitude after the unit stabilizes. For load increments of 5 %, 7.5 %, and 10 %, the rotor amplitude after the small oscillation in the x direction decreases by 14.1 %, 21.9 %, and 29.8 %, respectively. Similarly, in the y direction, the amplitude also decreases by 14.6 %, 22.4 %, and 29.8 %, respectively. Thus, it can be inferred that the unit's stability increases with the sudden increase in load.

The results can be explained as follows: when the load sudden increments or decrements, the rotational speed must be maintained at the rated speed. During this period, load variations affect the forces acting on the turbine blades. With an increase in load, the forces on the turbine runner blades rise, leading to an augmented damping effect and a consequent reduction in vibration. Conversely, during a decrease in load, the forces on the turbine runner blades diminish, resulting in reduced damping and an associated increase in vibration.

5. Transient response characteristics of the HTGU under different CLGVs

It is assumed that the GV opening changes from 1 to 0 to facilitate the comparison of the HTGS and shafting system's dynamic response processes during the GV closing process. Initial values are set to 1 for speed, discharge, head, and torque. The transient coupling model can be expressed as Eq. (28) when the GV is closed and the unit suddenly experiences a 100 % load reduction.

$$\begin{cases} \dot{x} = \frac{1}{T_{ab}}(m_t - e_n x - m_g) \\ \dot{q}_t = -\frac{1}{(0.17 + 0.4y)T_w}(q - 1.65y + 0.5y^2 + 0.15x) \\ \dot{h} = \frac{(0.17 + 0.4y)(q' - 1.65y' + yy' + 0.15x') - (0.4qy' - 0.66yy' + 0.2y'y^2 + 0.06xy')}{(0.17 + 0.4y)^2} \\ \dot{m}_t = \begin{cases} -0.16xx' - 0.3x' + 1.67y'h + 1.67yh' + 1.548[(1 - 0.6x)y' - 0.6x'(y - 1)], & (0 \leq y < 0.6) \\ -0.16xx' - 0.3x' + 1.67y'h + 1.67yh' + 1.2[(1 - 0.6x)y' - 0.6x'(y - 1)], & (0.6 \leq y < 0.85) \\ -0.16xx' - 0.3x' + 1.67y'h + 1.67yh' + 0.385[(1 - 0.6x)y' - 0.6x'(y - 1)], & (0.85 \leq y \leq 1) \end{cases} \end{cases} \quad (28)$$

(a) (b), x , h converges to the equilibrium point after several cycles of attenuation oscillation, and the response time is 33.5 s, which is similar to the process of the HTGU under load decrease. The radial amplitude of the rotor, described in Fig. 6 (c)–(e), gradually stabilizes again after

The transient response of the HTGU has been analyzed and studied under six two-stage CLGVs and five three-stage CLGVs, as presented in sections 5.1 and 5.2.

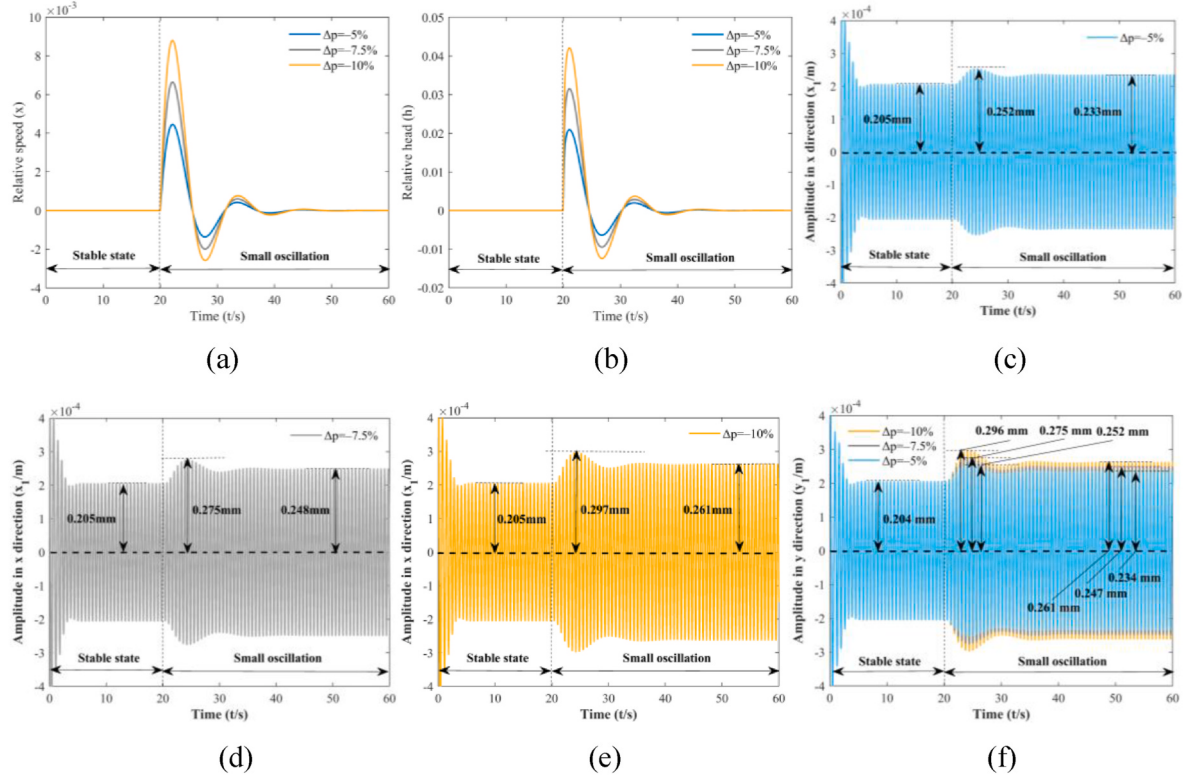


Fig. 5. Transient behaviors of relative speed, head, and rotor vibration after 5 %, 7.5 %, and 10 % load reduction.

5.1. Two-stage CLGV

The two-stage CLGV is a prevalent operational method in the engineering field [53]. Table 2 and Fig. 7 illustrate six two-stage CLGVs, with

Cases 1.1–1.3 representing fast-slow CLGVs and Cases 3.1–3.3 representing slow-fast CLGVs. The dynamic responses of speed, discharge, head, torque, and radial vibration are computed. The results are demonstrated in Fig. 8 (a)–(h).

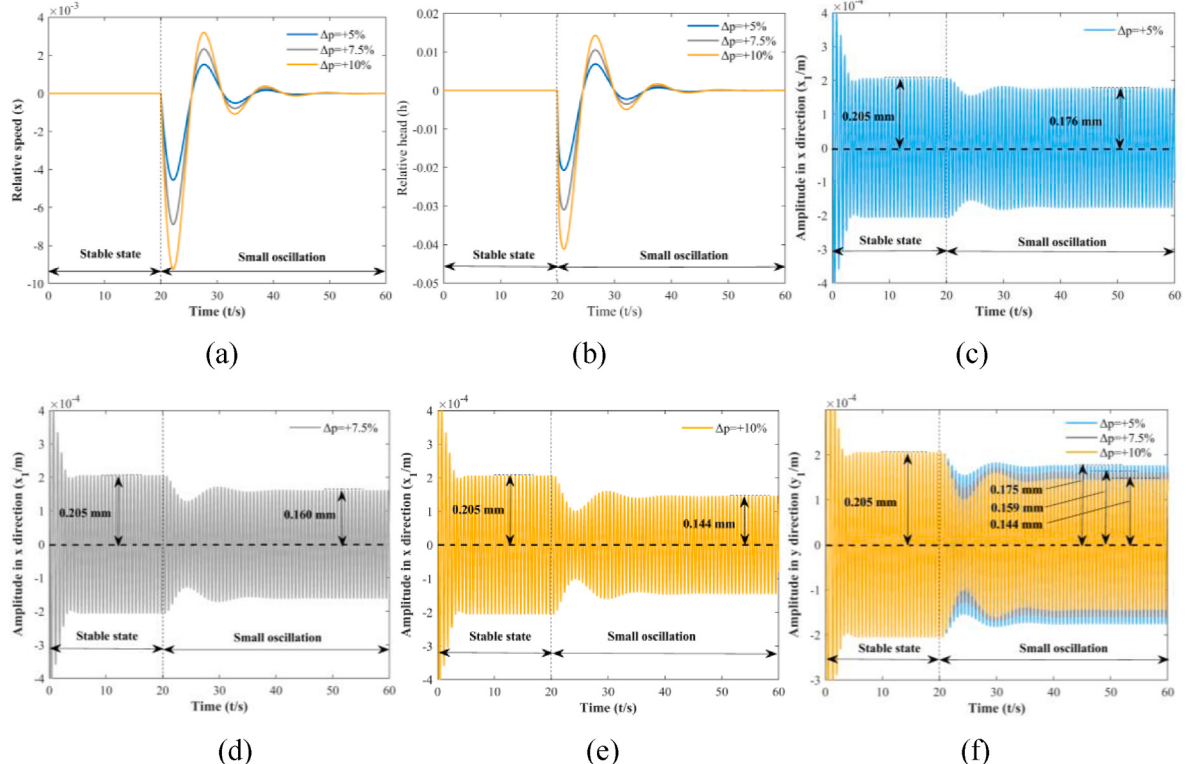
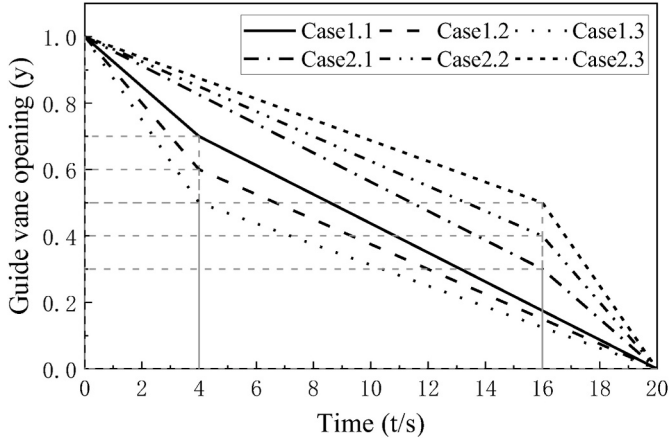


Fig. 6. Transient behaviors of relative speed, head, and rotor vibration after 5 %, 7.5 %, and 10 % load increase.

Table 2

Turning point parameter setting of Two-stage CLGV.

Case	GV opening of the turning point	Time of turning point	Total time
1.1	0.7	4	20
1.2	0.6	4	20
1.3	0.5	4	20
2.1	0.3	16	20
2.2	0.4	16	20
2.3	0.5	16	20

**Fig. 7.** Two-stage CLGV

According to Fig. 8(a)–(d), it can be inferred that the maximum relative speed for Case1.1, 1.2, and 1.3 occur at $t = 8.2$ s, 6.5 s, and 4.7 s, respectively, with maximum values of $x = 1.50$, 1.41 , and 1.34 , respectively. The head initially increases rapidly to reach the maximum value and then slowly decreases. The maximum head value for all three cases appears at the turning point $t = 4$ s, with values of $h = 1.16$, 1.22 , and 1.30 , respectively. The discharge and torque exhibit a similar decreasing trend until they become negative. Overall, under the fast-slow CLGV, it is observed that the faster the first section closing speed of the GV, the better the transient characteristics of the speed, but the worse the transient characteristics of the head.

The generator rotor and turbine in Case 1.1–1.3 exhibit radial

vibration as shown in Fig. 8 (e)–(h). In the generator rotor, as the GV is being closed, the amplitude in the x direction displays a characteristic of decrease-increase-decrease-increase, and the generator maximum amplitude attains values of 0.532 mm, 0.663 mm, and 1.021 mm, respectively. Similarly, the maximum amplitude in the y direction are 0.532 mm, 0.714 mm, and 1.033 mm, respectively. Broadly speaking, as the GV closes faster, the rotor's maximum radial vibration is reduced. In case of the turbine runner, owing to the misalignment of the shafting, the vibration of the rotor also displays a deviation that is not symmetrical about the coordinate axis, and the radial amplitude of the runner initially decreases and then increases.

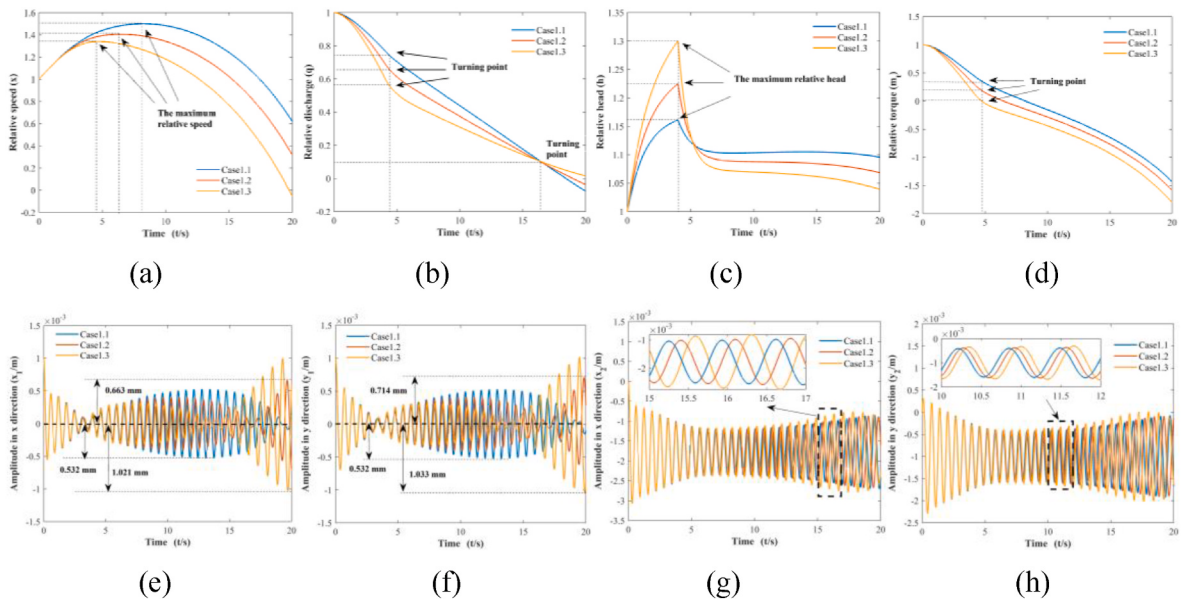
As shown in Fig. 9(a)–(d), the three cases, i.e., Case2.1, 2.2, and 2.3, attained their maximum relative speeds at $t = 10.6$, 11.8 , and 13.5 s, respectively, with x values of 1.66 , 1.72 , and 1.79 . During the closing process of the GV, the head experienced two rises. However, the maximum head occurred at $t = 20$ s for all three cases, with values of $h = 1.21$, 1.31 , and 1.41 . The dynamic response of discharge and torque is similar, as they decrease slowly at first, and then decrease rapidly at the turning point $t = 16$ s. In summary, under the slow-fast CLGVs, it can be observed that the slower the first stage GV is closed, the better the transient characteristics of the speed and head.

According to Fig. 9 (e)–(h), the amplitude of both the generator and runner decreases initially and then increases under the slow-fast CLGV. The generator's maximum amplitudes are 0.963 mm, 0.867 mm, and 0.714 mm (in the x direction); and 0.972 mm, 0.866 mm, and 0.716 mm (in the y direction). It is noteworthy the runner amplitude is generally higher than generator, and the maximum amplitude under different working conditions is similar.

5.2. Three-phase CLGVs

The three-stage CLGV has gained attention and is being discussed as it is found to have stronger control performance [29,30]. The effect of three-stage CLGVs on the HTGU's stability was analyzed by comparing the transient response characteristics under three CLGVs: CRC (Based on Lai et al.'s MOASA algorithm [41,54]), CDC, and CCC. The three-stage CLGV is illustrated in Fig. 10(a), while Fig. 10(b) and (c) depicts the five three-stage CLGVs proposed. Table 3 provides the specific parameters used in the analysis.

According to Fig. 11 (a) - (d), Case 3.1, Case 3.2, and Case 3.3

**Fig. 8.** The transient characteristics of relative speed, discharge, head, torque, and radial amplitude of generator and runner under the CLGVs of case1.1, case1.2 and case1.3.

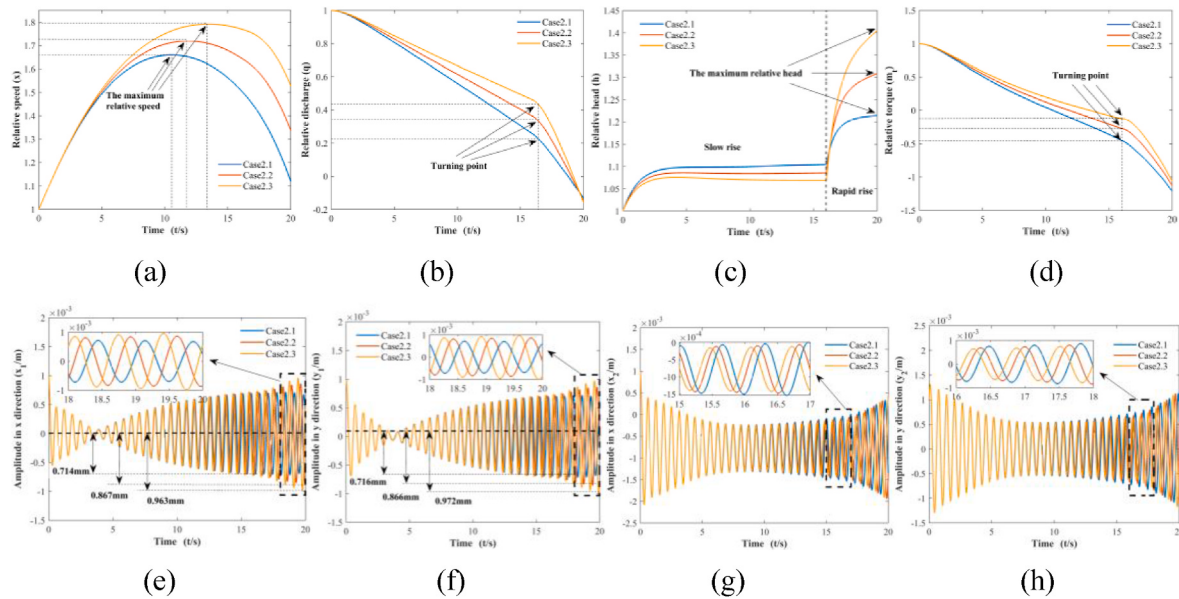


Fig. 9. The transient characteristics of relative speed, discharge, head, torque, and radial amplitude of generator and runner under the CLGVs of case2.1, case2.2 and case2.3.

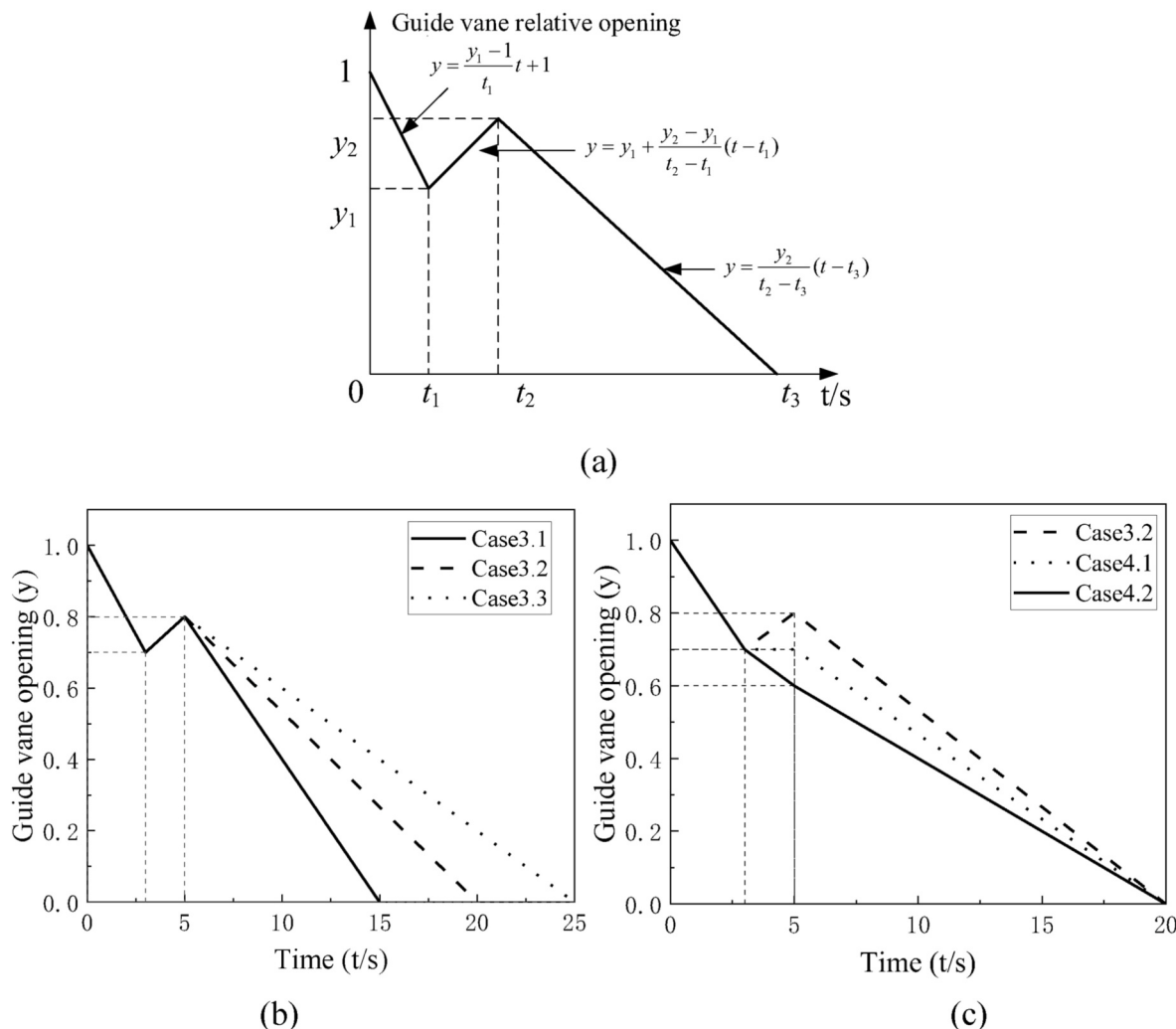


Fig. 10. Three-stage CLGV

Table 3

Turning point parameter setting of Three-stage CLGV.

Condition	GV opening of the first turning point	Time of first turning point	GV opening of the second turning point	Time of the second turning point	Total time
3.1	0.7	3	0.8	5	15
3.2	0.7	3	0.8	5	20
3.3	0.7	3	0.8	5	25
4.1	0.7	3	0.7	5	20
4.2	0.7	3	0.6	5	20

reached the maximum relative speed at $t = 8.9, 10.4, 11.7$ s, respectively, $x = 1.55, 1.59, 1.63$. During the GV closing process, the head experienced two rises, and the maximum relative head of Case 3.1

appeared in the second rise ($t = 15$ s), $h = 1.23$; the maximum relative head of Case 3.2 and Case 3.3 appeared in the first rise ($t = 3$ s), $h = 1.203$. The process of discharge change is similar to that of torque change. Speed and torque decrease more quickly with a shorter total closing time after $t = 5$ s. According to Fig. 11 (e)–(h), in the process of CRC CLGV, the amplitude of the generator is decreased-increased-decreased. According to Case 3.1–3.3, x amplitudes are 0.670 mm, 0.664 mm, and 0.667 mm; y amplitudes are 0.674 mm, 0.660 mm, and 0.664 mm. The maximum amplitude of the shafting system is affected little by the closing time of the third section. The amplitude of the turbine runner decreases first and then increases during the GV closing process, and the overall vibration amplitude of the runner is not only greater than that of the rotor, but also there is asymmetry. As a general rule, the shorter the closing time is of the GV third section, the better the dynamic response of the

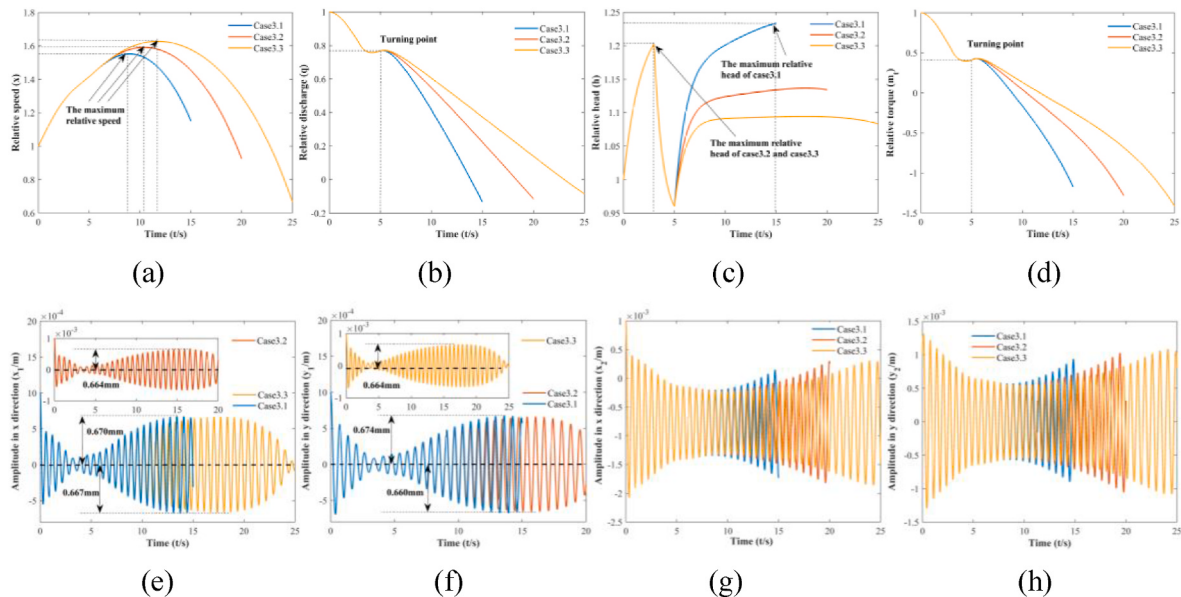


Fig. 11. The transient characteristics of relative speed, discharge, head, torque, and radial amplitude of generator and runner under the CLGVs of case3.1, case3.2 and case3.3.

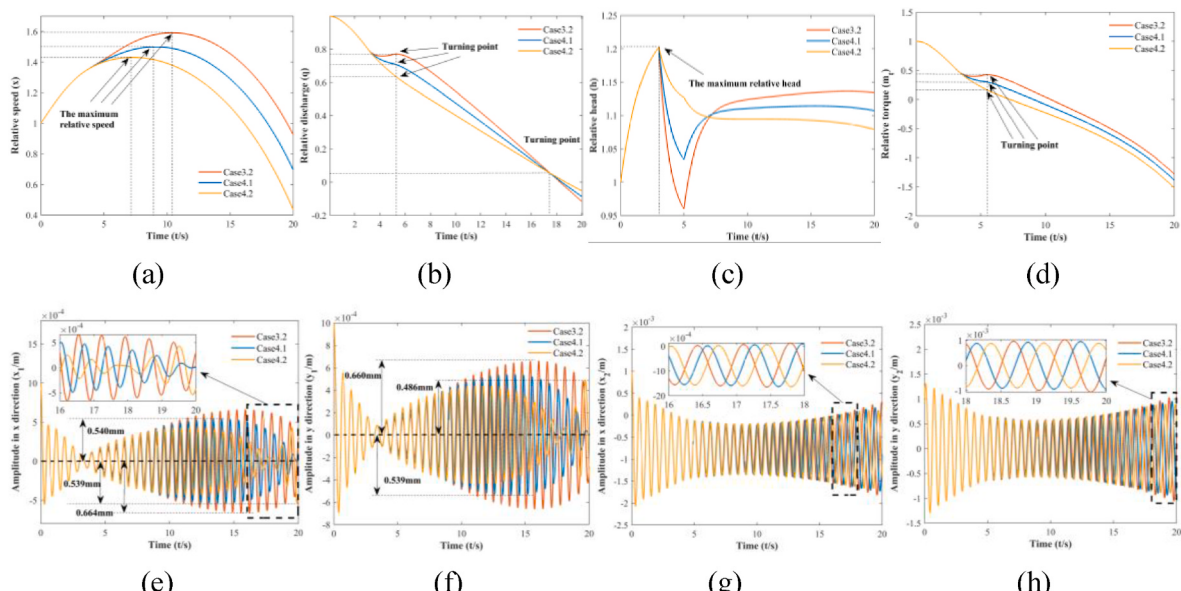


Fig. 12. The transient characteristics of relative speed, discharge, head, torque, and radial amplitude of generator and runner under the CLGVs of case3.2, case4.1 and case4.2.

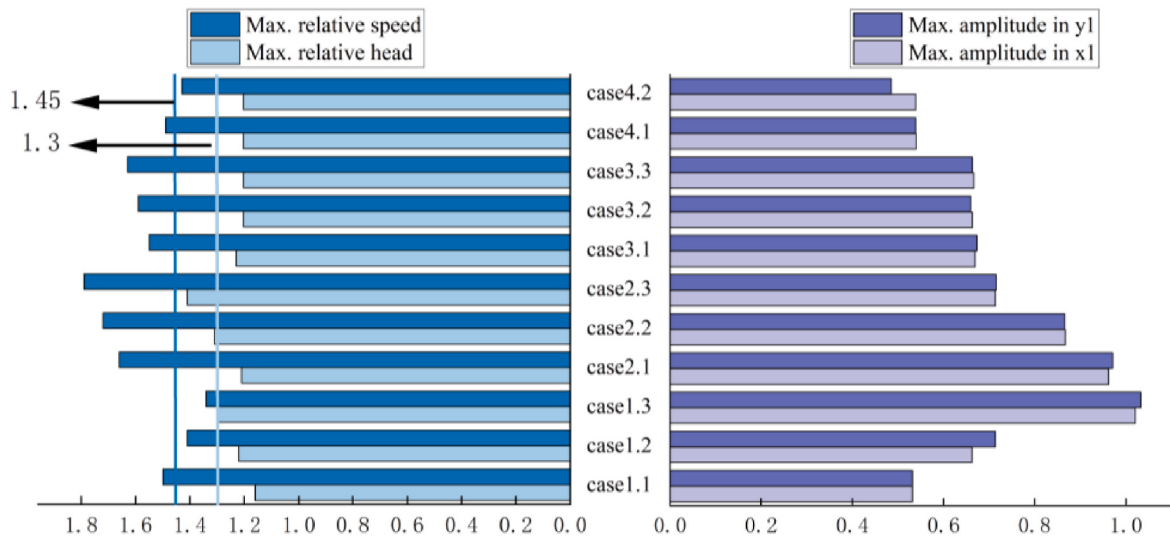


Fig. 13. Comparison of the maximum relative speed, head, and rotor amplitude under different GLGVs.

head is worse, and the discharge and torque decrease faster.

The dynamic response process of the HTGU under the CRC, CDC, and CCC GLGVs can be observed through Cases 3.2, 4.1, and 4.2 based on Fig. 12 (a) - (d). It is apparent that Case 3.2, 4.1, and 4.2 attained their maximum relative speed at $t = 10.41, 9.08$, and 7.27 , respectively, with corresponding values of x equaling $1.59, 1.49$, and 1.43 . During the head change process, Case 3.2 and Case 4.1 underwent two speed rises, while Case 4.2 only experienced a single speed rise. Despite the differences in transient response, the relative head in the three operating conditions attained its maximum after the first speed rise ($t = 3$ s), with a value of h equal to 1.203 . The flow and torque exhibit bifurcation at $t = 3$ s, but the changing trend remains consistent.

As shown in Fig. 12 (e)-(h), under Case 3.2 the rotor exhibits a maximum amplitude of 0.664 mm in the x and y directions. As compared to Case 3.2, Case 4.1 and Case 4.2 have smaller amplitudes, with maximum values of 0.540 mm and 0.539 mm in x direction, and 0.539 mm and 0.486 mm in y direction. Overall, the transient response characteristics of the HTGU are superior under Case 4.2 when compared to those observed under Case 3.2 and Case 4.1.

6. Analysis and discussion

The study of small vibration shows that the vibration of shafting system will be aggravated by the reduction of load, on the contrary, the sudden increase of load will enhance the stability of the system. Guo et al. [33,34] observed that the sudden increase of load greatly affected the stability of HTGU. The stronger the load, the more significant the vibration amplitude, which is consistent with the results of this paper.

The dynamic response of HTGU under eleven GLGVs was also examined. The comparative analysis of maximum relative speed, head, and rotor amplitude under these varied conditions is depicted in Fig. 13. According to NB/T 10342-2019, the speed variation $\Delta n_{\max} \leq 45\%$, $\Delta H_{\max} \leq 30\%$ when load rejection. As shown in Fig. 13, only Case1.2, Case1.3, and Case4.2 meet the requirements based on the constraints of speed and head. Regarding the transient characteristics of head, Case4.2 $>$ Case1.2 $>$ Case1.3, while according to the speed transient characteristics, case1.3 $>$ Case1.2 $>$ Case4.2. As for the maximum radial amplitude of the rotor, Case4.2 $>$ Case1.2 $>$ Case1.3 from smallest to largest.

Throughout the process of GV closure, the dynamic response exhibited by the HTGS is highly intricate, thereby contributing to the complexity observed in the shafting vibration characteristics. Nevertheless, it is noteworthy that during small oscillations, despite the alterations in turbine working conditions owing to load adjustments, the

unit consistently operates within the high-efficiency range. However, the unit could easily deviate from the optimal working condition area when the load suddenly increases or decreases too much. In this case, the unit's vibration will increase significantly due to hydraulic factors such as cavitation, noise, and tail vortex interference. As a result, considering the large oscillation, it is necessary to consider the vibration caused by hydraulic factors when the model deviates from the optimal working point.

7. Conclusion

This paper presents an improved surface-cluster method for establishing the transient turbine equation, and the conclusions are as follows:

- (1) The study establishes an improved transient turbine equation using the surface-cluster method. The equation is capable of capturing not only the transient features of HTGU during start-up but also those during small oscillations and shutdown.
- (2) During small oscillations, abrupt changes in load significantly impact the stability of the HTGU. A sudden decrease in load can result in increased vibration of the HTGU. Furthermore, the greater the load reduction, the more unstable the HTGU becomes due to increased vibration in the shaft system. Conversely, a sudden increase in load can decrease the amplitude of the shafting and improve its stability.
- (3) In two-stage GLGVs, the position of the turning point affects the maximum relative head, speed, and radial vibration. For the fast-slow GLGV, the maximum relative head and rotor radial vibration increase as the GV turning point opening decreases, whereas the speed change is in the opposite direction. Conversely, for the slow-fast GLGV, the maximum relative head and speed increase as the GV turning point opening decreases, while the maximum rotor radial amplitude is reduced.
- (4) Among all three-stage GLGVs, the CCC GLGV exhibits the best transient characteristics for the head, speed, and shafting amplitude. In contrast, for the CRC GLGV, the head's transient characteristics improve as GV closing time increases, while the speed are deteriorated.
- (5) Considering the hydraulic factors that cause vibration under large oscillations or load rejection when deviating from the optimal operating range is essential in coupling modeling. This is also a hot point where further efforts are needed and a challenge to be addressed.

CRediT authorship contribution statement

Jie Sun: Writing – original draft. **Chen Feng:** Writing – review & editing. **Yuquan Zhang:** Supervision. **Yuan Zheng:** Supervision.

Declaration of competing interest

The authors declare that they have no known competing financial interests or personal relationships that could have appeared to influence the work reported in this paper.

Data availability

No data was used for the research described in the article.

Acknowledgments

This work was supported by the National Natural Science Foundation of China (No. 52209110), the China Postdoctoral Science Foundation (2022M711017), and the Fundamental Research Funds for the Central Universities (B220202005).

References

- [1] C. Trivedi, M.J. Cervantes, O. Gunnar Dahlhaug, Numerical techniques applied to hydraulic turbines: a perspective review, *Appl. Mech. Rev.* 68 (1) (2016), 010802.
- [2] M.Z. Jacobson, M.A. Delucchi, M.A. Cameron, et al., Impacts of green new deal energy plans on grid stability, costs, jobs, health, and climate in 143 countries, *One Earth* 1 (4) (2019) 449–463.
- [3] P. Matschoss, B. Bayer, H. Thomas, et al., The German incentive regulation and its practical impact on the grid integration of renewable energy systems, *Renew. Energy* 134 (2019) 727–738.
- [4] J. Li, S. Chen, Y. Wu, et al., How to make better use of intermittent and variable energy? A review of wind and photovoltaic power consumption in China, *Renew. Sustain. Energy Rev.* 137 (2021), 110626.
- [5] Q. Zhang, X. Wang, T. Yang, et al., Research on scheduling optimisation for an integrated system of wind-photovoltaic-hydro-pumped storage, *J. Eng.* 2017 (13) (2017) 1210–1214.
- [6] X. Ji, H. Wang, L. He, New energy grid-connected power quality management system based on internet of things, *Sustain. Comput.: Informatic. Syst.* 30 (2021), 100460.
- [7] D. Li, X. Fu, Z. Zuo, et al., Investigation methods for analysis of transient phenomena concerning design and operation of hydraulic-machine systems—a review, *Renew. Sustain. Energy Rev.* 101 (2019) 26–46.
- [8] Z. Zuo, H. Fan, S. Liu, et al., S-shaped characteristics on the performance curves of pump-turbines in turbine mode – a review, *Renew. Sustain. Energy Rev.* 60 (2016) 836–851.
- [9] H. Zhang, D. Chen, C. Wu, et al., Dynamic modeling and dynamical analysis of pump-turbines in S-shaped regions during runaway operation, *Energy Convers. Manag.* 138 (2017) 375–382.
- [10] K. Kan, M. Binama, H. Chen, et al., Pump as turbine cavitation performance for both conventional and reverse operating modes: a review, *Renew. Sustain. Energy Rev.* 168 (2022), 112786.
- [11] K. Kan, H. Chen, Y. Zheng, et al., Transient characteristics during power-off process in a shaft extension tubular pump by using a suitable numerical model, *Renew. Energy* 164 (2021) 109–121.
- [12] A.J. Laguna, Modeling and analysis of an offshore wind turbine with fluid power transmission for centralized electricity generation, *J. Comput. Nonlinear Dynam.* 10 (4) (2015), 041002.
- [13] F. Botero, V. Hasmatuchi, S. Roth, et al., Non-intrusive detection of rotating stall in pump-turbines, *Mech. Syst. Signal Process.* 48 (1–2) (2014) 162–173.
- [14] H. Li, D. Chen, H. Zhang, et al., Hamiltonian analysis of a hydro-energy generation system in the transient of sudden load increasing, *Appl. Energy* 185 (2017) 244–253.
- [15] B. Xu, X. Luo, M. Egusquiza, et al., Nonlinear modal interaction analysis and vibration characteristics of a francis hydro-turbine generator unit, *Renew. Energy* 168 (2021) 854–864.
- [16] H. Zhang, D. Chen, B. Xu, et al., Dynamic analysis of a pumped-storage hydropower plant with random power load, *Mech. Syst. Signal Process.* 100 (2018) 524–533.
- [17] D. Chen, C. Ding, Y. Do, et al., Nonlinear dynamic analysis for a Francis hydro-turbine governing system and its control, *J. Franklin Inst.* 351 (9) (2014) 4596–4618.
- [18] C. Li, L. Chang, Z. Huang, et al., Parameter identification of a nonlinear model of hydraulic turbine governing system with an elastic water hammer based on a modified gravitational search algorithm, *Eng. Appl. Artif. Intell.* 50 (2016) 177–191.
- [19] B. Guo, B. Xu, D. Chen, et al., Dynamic modeling and energy distribution analysis in a hydroelectric generating system considering the stochastic turbine flow, *Int. J. Electr. Power Energy Syst.* 103 (2018) 611–621.
- [20] H. Zhang, D. Chen, C. Wu, et al., Dynamics analysis of the fast-slow hydro-turbine governing system with different time-scale coupling, *Commun. Nonlinear Sci. Numer. Simulat.* 54 (2018) 136–147.
- [21] X. Gao, D. Chen, H. Zhang, et al., Nonlinear fast-slow dynamics of a coupled fractional order hydropower generation system, *Chin. Phys. B* 27 (12) (2018), 128202.
- [22] H. Zhang, D. Chen, P. Guo, et al., A novel surface-cluster approach towards transient modeling of hydro-turbine governing systems in the start-up process, *Energy Convers. Manag.* 165 (2018) 861–868.
- [23] Q. Wu, L. Zhang, Z. Ma, A model establishment and numerical simulation of dynamic coupled hydraulic-mechanical-electric-structural system for hydropower station, *Nonlinear Dynam.* 87 (1) (2017) 459–474.
- [24] L.L. Earles, A.B. Palazzolo, R.W. Armentrout, A finite element approach to pad flexibility effects in tilt pad journal bearings: Part I—single pad analysis, *J. Tribol.* 112 (2) (1990) 169–176.
- [25] L.L. Earles, A.B. Palazzolo, R.W. Armentrout, A finite element approach to pad flexibility effects in tilt pad journal bearings: Part II—assembled bearing and system analysis, *J. Tribol.* 112 (2) (1990) 178–182.
- [26] M. Karlsson, J.-O. Aidanpää, R. Perers, et al., Rotor dynamic analysis of an eccentric hydropower generator with damper winding for reactive load, *J. Appl. Mech.* 74 (6) (2007) 1178–1186.
- [27] W. Sun, Z. Guo, Mathematical modeling and nonlinear vibration analysis of a coupled hydro-generator shaft-foundation system, *Commun. Nonlinear Sci. Numer. Simulat.* 98 (2021), 105776.
- [28] Y. Shi, J. Zhou, X. Lai, et al., Stability and sensitivity analysis of the bending-torsional coupled vibration with the arcuate whirl of hydro-turbine generator unit, *Mech. Syst. Signal Process.* 149 (2021), 107306.
- [29] L. Zhang, H. Tang, T. Sun, et al., Vibration characteristics analysis of shaft system for bulb hydroelectric generating unit based on magnetorheological fluid damper, *Chaos, Solit. Fractals* 163 (2022), 112559.
- [30] X. Xie, M. Ren, H. Zheng, et al., Active vibration control of a time-varying shafting system using an adaptive algorithm with online auxiliary filter estimation, *J. Sound Vib.* 513 (2021), 116430.
- [31] H. Li, B. Xu, A. Riasi, et al., Performance evaluation in enabling safety for a hydropower generation system, *Renew. Energy* 143 (2019) 1628–1642.
- [32] Y. Shi, J. Zhou, Stability and sensitivity analyses and multi-objective optimization control of the hydro-turbine generator unit, *Nonlinear Dynam.* 107 (3) (2022) 2245–2273.
- [33] B. Guo, B. Xu, D. Chen, et al., Vibration characteristics of a hydroelectric generating system during the load rejection process, *J. Comput. Nonlinear Dynam.* 14 (7) (2019), 071006.
- [34] Y. Guo, X. Liang, Z. Niu, et al., Vibration characteristics of a hydroelectric generating system with different hydraulic-mechanical-electric parameters in a sudden load increasing process[J]. *Energies, Multidisciplin. Digital Pub. Instit.* 14 (21) (2021) 7319.
- [35] W. Guo, J. Yang, M. Wang, et al., Nonlinear modeling and stability analysis of hydro-turbine governing system with sloping ceiling tailrace tunnel under load disturbance, *Energy Convers. Manag.* 106 (2015) 127–138.
- [36] L. Wang, K. Zhang, W. Zhao, Nonlinear modeling of dynamic characteristics of pump-turbine[J]. *Energies, Multidisciplin. Digital Pub. Instit.* 15 (1) (2022) 297.
- [37] H. Zhuang, Transient Dynamical Modeling and Stability Analysis of Hydroelectric Power Systems [D], Northwest A&F University, 2019.
- [38] L. Yongling, H. Yu, M. Jin, et al., Active disturbance rejection controller for hydraulic turbine generator system[A]. Proceedings of the 31st Chinese Control Conference[C], 2012, pp. 4684–4688.
- [39] H. Zhang, D. Chen, B. Xu, et al., Nonlinear modeling and dynamic analysis of hydro-turbine governing system in the process of load rejection transient, *Energy Convers. Manag.* 90 (2015) 128–137.
- [40] W. Guo, J. Yang, Hopf bifurcation control of hydro-turbine governing system with sloping ceiling tailrace tunnel using nonlinear state feedback, *Chaos, Solitons & Fractals* 104 (2017) 426–434.
- [41] X.J. Lai, Research on Stability and Transient Process Control Optimization of Hydro-Turbine Governing System, Huazhong University of Science and Technology, 2021.
- [42] B. Xu, D. Chen, H. Zhang, et al., Dynamic analysis and modeling of a novel fractional-order hydro-turbine-generator unit, *Nonlinear Dynam.* 81 (3) (2015) 1263–1274.
- [43] Y. Shi, J. Shen, W. Guo, et al., The nonlinear dynamic characteristics analysis and vibration reduction control of the shafting system of a hydropower unit, *Int. J. Non Lin. Mech.* 146 (2022), 104166.
- [44] K. Zhuang, C. Gao, Z. Li, et al., Dynamic analyses of the hydro-turbine generator shafting system considering the hydraulic instability, *Energies* 11 (10) (2018) 2862.
- [45] P. Gao, L. Hou, R. Yang, et al., Local defect modelling and nonlinear dynamic analysis for the inter-shaft bearing in a dual-rotor system, *Appl. Math. Model.* 68 (2019) 29–47.
- [46] The stability analysis and nonlinear vibration control of shaft system for hydraulic generating set under multi-source excitation considering effects of dynamic and static eccentricities, in: Communications in Nonlinear Science and Numerical Simulation, vol. 121, Elsevier, 2023, 107230.
- [47] H. Ma, H. Li, X. Zhao, et al., Effects of eccentric phase difference between two discs on oil-film instability in a rotor-bearing system, *Mech. Syst. Signal Process.* 41 (1–2) (2013) 526–545.
- [48] Y. Shi, J. Zhou, J. Huang, et al., A vibration fault identification framework for shafting systems of hydropower units: nonlinear modeling, signal processing, and

- holographic identification, Sensor., Multidisciplin. Digital Pub. Institut. 22 (11) (2022) 4266.
- [49] B. Xu, D. Chen, P. Behrens, et al., Modeling oscillation modal interaction in a hydroelectric generating system, Energy Convers. Manag. 174 (2018) 208–217.
- [50] W. Zhang, Research on Dynamics of Shaft System of Hydro-Electric Generating Set, Dalian University of Technology, 2008.
- [51] B. Xu, D. Yan, D. Chen, et al., Sensitivity analysis of a Pelton hydropower station based on a novel approach of turbine torque, Energy Convers. Manag. 148 (2017) 785–800.
- [52] B. Xu, D. Chen, H. Zhang, et al., Shaft mis-alignment induced vibration of a hydraulic turbine generating system considering parametric uncertainties, J. Sound Vib. 435 (2018) 74–90.
- [53] Z. Zhao, J. Yang, W. Yang, et al., A coordinated optimization framework for flexible operation of pumped storage hydropower system: nonlinear modeling, strategy optimization and decision making, Energy Convers. Manag. 194 (2019) 75–93.
- [54] X. Lai, C. Li, J. Zhou, et al., Multi-objective optimization of the closure law of guide vanes for pumped storage units, Renew. Energy 139 (2019) 302–312.